



Article

Inkjet Printing on a New Flexible Ceramic Substrate for Internet of Things (IoT) Applications

Sharadindu Gopal Kirtania ¹, Manjurul Ahsan Riheen ¹, Sun Ung Kim ¹ , Karthik Sekhar ², Anna Wisniewska ¹ and Praveen Kumar Sekhar ^{1,*}

¹ School of Engineering and Computer Science, Washington State University, Vancouver, WA 98686, USA; sharadindu.kirtania@wsu.edu (S.G.K.); m.riheen@wsu.edu (M.A.R.); sunung.kim@wsu.edu (S.U.K.); anna.wisniewska@wsu.edu (A.W.)

² Department of ECE, Faculty of Engineering and Technology, SRM Institute of Science and Technology, Vadapalani Campus, No.1, Jawaharlal Nehru Road, Vadapalani, Chennai, TN 600026, India; karthiks1@srmist.edu.in

* Correspondence: praveen.sekhar@wsu.edu

Received: 19 August 2020; Accepted: 6 September 2020; Published: 8 September 2020



Abstract: In this article, the optimization of printing properties on a new, flexible ceramic substrate is reported for sensing and antenna applications encompassing internet of things (IoT) devices. E-Strate[®] is a commercially available, non-rigid, thin ceramic substrate for implementing in room temperature and high-temperature devices. In this substrate, the printing parameters like drop spacing, number of printed layers, sintering temperature, and sintering time were varied to ensure an electrically conductive and repeatable pattern. The test patterns were printed using silver nanoparticle ink and a Dimatix 2831 inkjet printer. Electrical conductivity, high-temperature tolerance, bending, and adhesion were investigated on the printed samples. The three-factor factorial design analysis showed that the number of printed layers, sintering temperature, sintering time, and their interactions were significant factors affecting electrical conductivity. The optimum printing parameters for the thin E-Strate[®] substrate were found to be 20 μm drop spacing, three layers of printing, and 300 $^{\circ}\text{C}$ sintering temperature for 30 min. The high-temperature tolerance test indicated a stable pattern without any electrical degradation. Repetitive bending, adhesion test, and ASTM tape tests showed adequate mechanical stability of the pattern. These results will provide insight for investigators interested in fabricating new IoT devices.

Keywords: printing parameters; sintering; curing; electrical resistivity analysis of silver nanoparticles; IoT; bending analysis; analysis of variance (ANOVA)

1. Introduction

There is an unmet need for integrated, inexpensive, and conformal devices with a smaller footprint in the era of the internet of things (IoT) [1–3]. In particular, the IoT framework in nuclear power plants [4], industrial compressors [5], automotive industry [6], oil refineries [7], aerospace propulsion systems [8], etc. requires wireless sensing systems to monitor physical and chemical parameters accurately. To improve efficiency, safety, and diagnostics, hundreds of these wireless sensors are required to fit in critical areas, planar or non-planar in nature. In addition, federal agencies in the U.S [9] and industry are looking for an integrated, high-temperature operable, and flexible wireless sensor system solution [10]. In this context, the need for a flexible substrate conducive to room temperature and high-temperature operation becomes relevant.

Commonly used substrates for flexible devices such as sensors and antenna include different types of polymer and paper substrates [11]. While the paper and polymer substrates are suitable

for room temperature device operation [12], high-temperature operation require ceramic substrates. E-strate[®] is a commercially available thin, flexible ceramic substrate that enables device operation at room temperature and high temperature (up to 1000 °C).

E-strate[®] is made of 3 mol% partially yttria-stabilized zirconia (3YSZ) [13]. Due to its high dielectric constant, low thermal conductivity, superior mechanical properties, and tolerance to high temperatures, E-strate[®] has enabled radio frequency, photonics, chemical sensing, and renewable energy applications [14–17]. Various metallization techniques have been investigated on this substrate for device fabrication, while inkjet printing for device fabrication has been relatively unexplored.

Inkjet printing technology is a simple yet effective method to fabricate sensors, antennas, integrated circuits, batteries, displays, Radio-frequency identification (RFID) tags, thin-film transistors, and many other devices [18]. Fabricating devices using inkjet printing offers a precise definition of intricate patterns on the substrate. Typically, three types of ink are used in inkjet printing. They are metal nanoparticles (NPs) like silver (Ag), copper (Cu), or gold (Au), metal-organic decomposition (MOD) ink [19], and conductive polymers [20]. Among metal NP inks, silver has the lowest bulk resistivity, $1.59 \times 10^{-8} \Omega\text{-m}$ [21]. The printed pattern of Ag NPs on a substrate needs sintering for decomposing the protective agents from the surfaces of Ag NPs. Sintering ensures direct physical contact between Ag NPs and sets up a dense and conductive system throughout the printed pattern [22]. Hence, the sintering temperature and sintering time need to be carefully chosen.

Lower sintering temperature fails to yield a dense and highly conductive printed feature while a higher value degrades the pattern. Further, appropriate sintering time is critical for optimum conductivity of the printed pattern [23]. Optimization of the printer parameters for the selected ink and substrate combination is mandatory to guarantee high printing quality, as inks with varying viscosity and surface tension interact differently with various substrates. The authors have prior experience in optimizing printing properties on different substrates [24,25]. A fundamental requirement for robust device implementation is the device integrity at room temperature and high temperature in addition to flat and bent conditions. Hence, a reliable inkjet printing process is essential for large scale device fabrication.

In this context, the optimum printing parameters on thin E-strate[®] are determined in order to obtain a highly conductive and mechanically stable printed pattern, a critical requirement of flexible devices. The printing parameters such as drop spacing, the number of printed layers, sintering temperature, and sintering duration were investigated. The electrical conductivity of the printed samples was inspected to ensure the quality of printing. To assess flexibility and pattern durability, the authors performed bending and adhesion tests.

2. Experimental

2.1. Materials

Commercially available Ag NP ink was purchased from Novacentrix[®] (Model: Metalon-JS-B25HV). This is a water-based Ag ink with 25 wt% Ag content with viscosity is 8–10 cp and surface tension 30–32 dyne/cm. The relative density of the ink is 1.2–1.4. The z-average particle size for this ink is 60–80 nm. The thin E-strate[®] was purchased from ENrG Inc. The substrate thickness is 40 μm , and the dimension of the substrate is 27 mm \times 47 mm.

2.2. Printing of Test Pattern

A Fujifilm Dimatix Materials Printer (DMP-2831) was used to print the pattern on thin E-strate[®]. 10 pL cartridges were used for the experiment. The primary objective of the optimization is to create a consistent and straight away droplet at a velocity within the range of 5.5–6 m/s from the selected nozzles so that the jetted drops attach well to the thin E-strate[®] surface. The droplets of ink were inspected using the drop watcher of Drop Manager Software of DMP. The jetting waveform, the jetting voltage, the jetting frequency, the cartridge temperature, the platen temperature, and the resolution

of the pattern dictate the printing quality of the inkjet printer [11]. Table 1 shows the values of the parameters mentioned above. Figure 1 shows the drop formation from a single nozzle using the drop watcher camera. The jetting voltage controls the speed of the droplet firing. The printer height from the substrate affects the formation of the satellite droplets (Figure 1), printing accuracy and resolution. Initially, there were some satellite droplets within the first 30 to 50 μs . However, at a substrate height of 550 μm (around 80 μs), the droplets were seen to be steady and satellite droplets coalesced into a single droplet.

Table 1. Printing specifications.

Parameter	Value
Jetting Voltage (V)	15.4
Jetting Frequency (kHz)	4.4
Drop Size (pL)	10
Printing Print Height (μm)	550
Cartridge Temperature ($^{\circ}\text{C}$)	31
Platen Temperature ($^{\circ}\text{C}$)	50

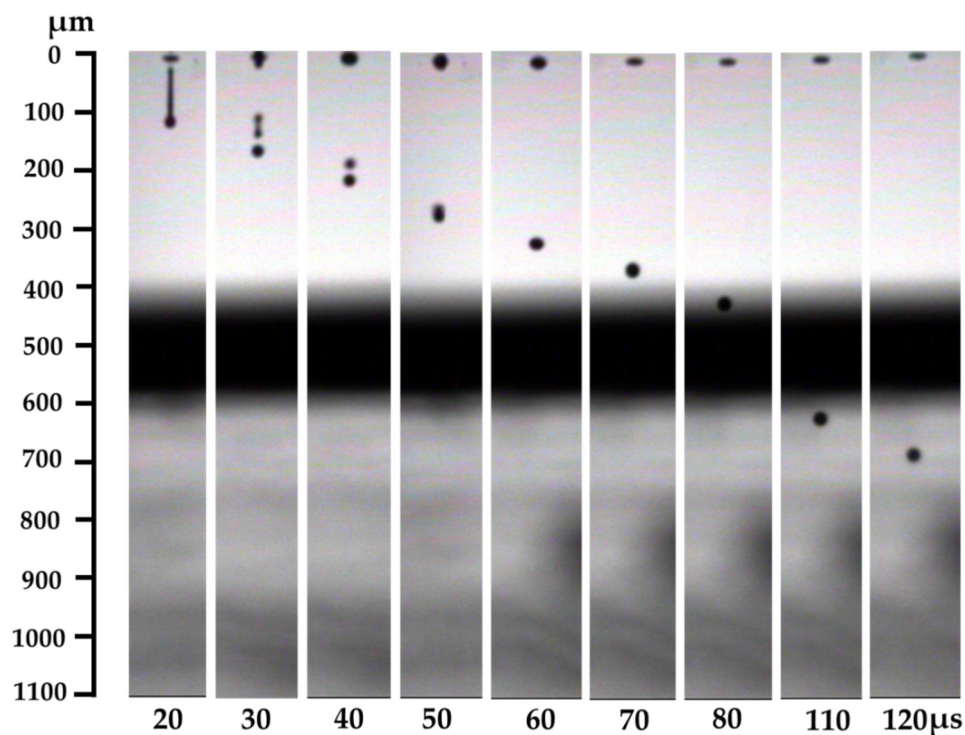


Figure 1. Drop formation of ink from a single nozzle in different time frame. Satellite droplets were formed at 30 μs and retracted after 50 μs . (For 90 and 100 μs , the droplet was in the shadowed part, which was not given in the figure).

A square test pattern of dimension 15 mm \times 15 mm was designed in ANSYS EM software and uploaded in the DMP. The printing parameters, such as the number of printing layers, sintering temperature, sintering time, and drop spacing (shown in Table 2) were varied, and the resistivity was recorded. The initial values of these parameters were decided based on trial and inspection.

Table 2. Experimental printing parameters.

Parameter	Value	Unit
Drop Spacing	15, 20, 25	μm
Printed Layer Numbers	1, 2, 3, 4	
Sintering Temperature	250, 300, 350, 400	°C
Sintering Time	10, 20, 30, 40	min

2.3. Post-Processing and Resistivity Measurement

Tables 1 and 2 show the printing specifications and experimental printing parameters, respectively.

The printed samples were sintered using a hot air gun (Model: Kendal 898D⁺). Printed test patterns were very thin, and their resistances can be considered as sheet resistances, which were measured using the four-point probe method [26]. The formula below was applied to calculate the electrical resistivity (ρ):

$$\rho = (R_s \times t) \Omega\text{-cm} \quad (1)$$

where R_s = the sheet resistance of the printed pattern (Ω/sq) and t = thickness of the Ag ink layer (cm). Jandal's four-point probe was used to measure the sheet resistance. As thin E-strate[®] is a non-porous substrate, the ink does not get absorbed on the surface. As per the material datasheet of Novacentrix[®], high-temperature sintering (250 °C or greater) is recommended for the proper adhesion of ink to the substrate.

2.4. Surface Characterization

Scanning electron microscope (SEM) Quanta 3D 200i was used to measure the printed layer thickness. The test specimens were inspected using Alpha-Step[®] D-300 Stylus Profiler to investigate the surface roughness and the uniformity of the printed pattern. The surface morphology of the different layered printed specimens was examined using the SEM.

2.5. High-Temperature Tolerance Test

The high-temperature tolerance of the printed pattern on thin E-strate[®] was tested via the fabrication of a capacitive interdigitated (IDT) pattern. The IDT pattern was designed and simulated an IDT capacitor on COMSOL Multiphysics 5.4. The capacitance value was found to be 48 pF based on the simulation. Then, the IDT structure was printed on thin E-strate[®] and sintered it at 300 °C for 30 min. The capacitance was measured using the LCR meter, Model: Amprobe LCR55A. Then, the printed capacitor was heated at 500 °C for 1 h, and the capacitance value was measured after the substrate was cooled down.

2.6. Flexibility and Adhesion Test

The flexible substrate was subjected to repeated bending (100 cycles) to assess the mechanical and electrical integrity of the patterns as it would be the case in real-time applications. To check the flexibility of thin E-strate[®], repetitive tensile bending, and adhesion test (100 runs) of the printed pattern were carried out. Repetitive bending test was performed by folding the printed pattern around different radii of curved structure [27,28]. The printed rectangular pattern was bent around the two cylindrical shapes of diameter 53 mm (Figure 2), and 64 mm. The ASTM standard tape test was used to check the adhesion strength of the printed pattern with the substrate.

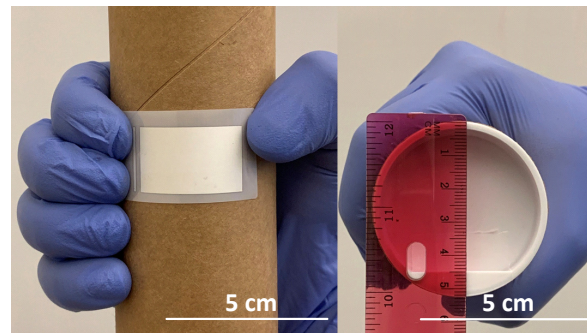


Figure 2. Flexibility test on a printed pattern.

3. Results and Discussion

3.1. Electrical Conductivity

The pattern printed with drop spacing (DS) of $15\ \mu\text{m}$ (1693 DPI), $20\ \mu\text{m}$ (1270 DPI), and $25\ \mu\text{m}$ (1016 DPI) were inspected using the Fiducial Camera of DMP. Figure 3 shows the surface of the pattern printed using different drop spacing. A sharp edge quality of the printed pattern at $20\ \mu\text{m}$ DS was observed.

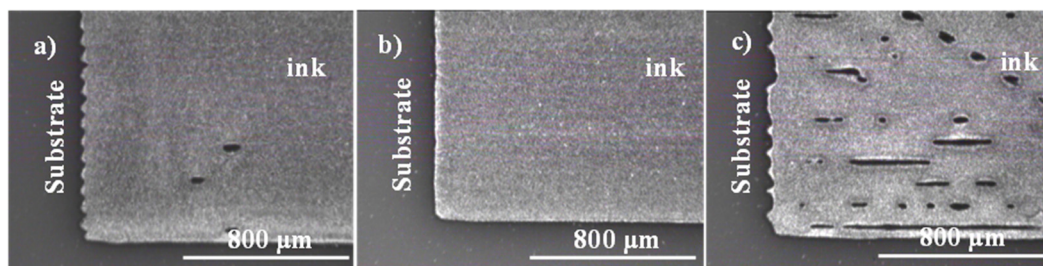


Figure 3. Inkjet-printed pattern: (a) $15\ \mu\text{m}$ drop spacing, (b) $20\ \mu\text{m}$ drop spacing, and (c) $25\ \mu\text{m}$ drop spacing.

For $15\ \mu\text{m}$ drop spacing, the droplets seem to become too close, which results in more ink spreading and degradation of the printed pattern edges [29]. On the other hand, a higher DS ($25\ \mu\text{m}$) seems to create an irregular printed pattern with higher resistivity values.

Hence, the $20\ \mu\text{m}$ DS was selected as the optimum DS. After determining the optimum DS, the correlation of the resistivity with the number of printing layers, sintering temperature, sintering time was studied. The measured resistivity as a function of sintering temperature, sintering time, and the number of printed layers is presented in Table 3. A three factorial design based statistical approach was pursued to determine the significance of sintering temperature, the number of printing layers, sintering time, and their interaction on the resistivity of the printed sample. The data for a single layer pattern is omitted from the analysis due to numerous outliers in the resistivity values (attributed to pinholes and irregular patterns). Each data point was repeated, which is indicated by 'run 1' and 'run 2' column. From Table 3, it can be inferred that resistivity values decrease with sintering time. The three-factor analysis of variance (ANOVA) is summarized in Table 4. The analysis reveals that the number of printing layers, sintering temperature, and sintering time affect resistivity significantly.

Table 3. Measured resistivity as a function of sintering time, sintering temperature, and the number of printed layers.

Sintering Temperature (°C) (A)	Resistivity ($\mu\Omega\text{-cm}$)						
	Number of Layers (B)	2 L		3 L		4 L	
	Sintering Time (C)	run-1	run-2	run-1	run-2	run-1	run-2
250	10	113.52	112.24	12.65	13.59	13.59	12.65
	20	30.92	30.57	8.66	9.47	7.55	8.66
	30	28.02	29.01	7.33	6.66	6.8	7.04
	40	26.57	26.57	5.33	5.33	6.04	6.66
300	10	5.8	6.16	4.66	4.68	3.78	3.78
	20	5.31	5.81	4	4.1	3.4	3.4
	30	5.31	5.31	3.33	3.33	3.02	3.05
	40	5.31	5.31	3.33	3.33	3.02	3.05
350	10	6.16	6.16	4.75	4.58	4.29	4.55
	20	5.81	6.12	4.25	4.2	4.21	4.33
	30	5.21	5.2	3.33	3.33	3.35	3.33
	40	5.12	5.15	3.33	3.33	3.33	3.33
400	10	5.8	6.66	4.66	5.33	4.15	4.33
	20	5.07	5.15	4	4.66	3.78	3.78
	30	5.07	5.07	3.33	3.33	3.78	3.53
	40	5.07	5.07	3.33	3.33	3.78	3.87

Table 4. Analysis of Variance (ANOVA) chart.

Source of Variation	Sum of Squares (SS)	Degrees of Freedom (DF)	Mean Square (MS)	F _{critical}	F	p-Values
Sintering Temperature (A)	5796.77	3	1932.26	2.80	19,267.78	$p \ll 0.05$
Number of printing layers (B)	2846.73	2	1423.36	3.19	14,193.29	$p \ll 0.05$
Sintering Time (C)	1372.86	3	457.62	2.80	4563.21	$p \ll 0.05$
AB	6190.36	6	1031.73	2.29	10,288.02	$p \ll 0.05$
CA	3978.44	9	442.05	2.08	4407.96	$p \ll 0.05$
BC	1525.08	6	254.18	2.29	2534.59	$p \ll 0.05$
ABC	3935.35	18	218.63	1.82	2180.11	$p \ll 0.05$
Error	4.81	48	0.10			
Total	25,650.40	95				

Further, their mutual interactions seem to influence resistivity. As the F-values for printing layers and temperatures and their interaction are very high compared to other factors, they affect resistivity more significantly. Figure 4 shows an array of graphs highlighting electrical resistivity as a function of sintering time for different sintering temperatures. As the patterns require thermal sintering for significant electrical conductivity, no resistivity was measured before sintering. After minimum sintering of 10 min, the readings for resistivity were recorded. The optimum resistivity value was observed to be $3.33 \mu\Omega\text{-cm}$ (desired value) for 3 L printing at 300°C sintering temperature for 30 min of sintering. With an increase in sintering temperature from 250°C to 400°C , the sintering time to get the optimum value of resistivity seems to reduce. Before thermal curing, there is no physical contact between the silver nanoparticles, and the printed patterns show no conductivity.

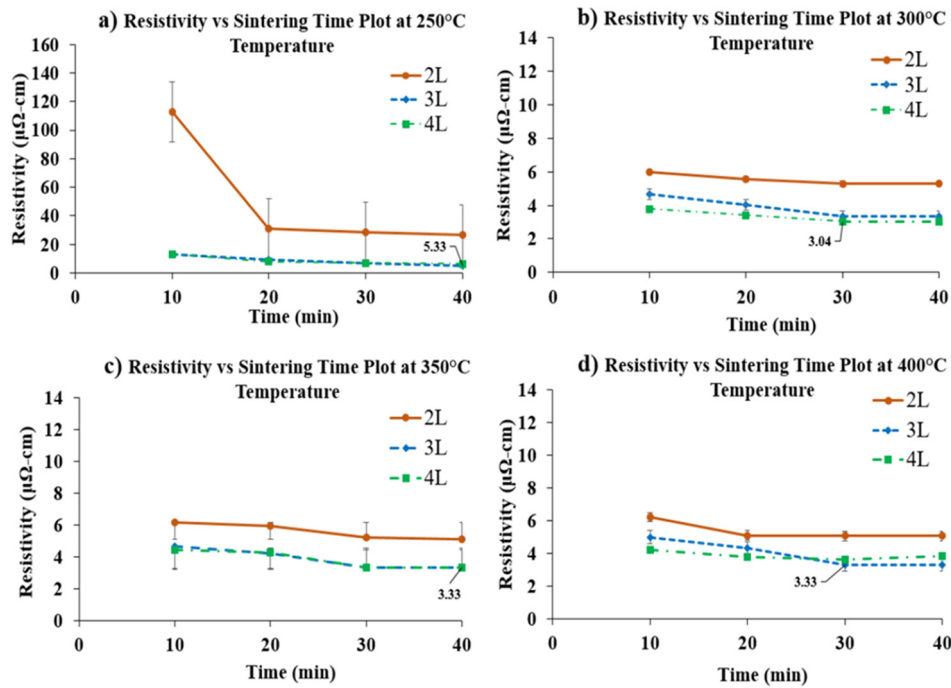


Figure 4. Resistivity value as a function of sintering time at different sintering temperatures: (a) 250 °C, (b) 300 °C, (c) 350 °C, (d) 400 °C.

Heat is required to decompose the organic solvent and create metallic contact between the particles to form a conductive feature. These changes in resistance of the printed patterns arise from a material transport process based on the atomic diffusion driven by the reduction of interfacial energy [30]. For better understanding, a schematic of two interacting nanoparticles with possible diffusion paths during sintering is shown in Figure 5.

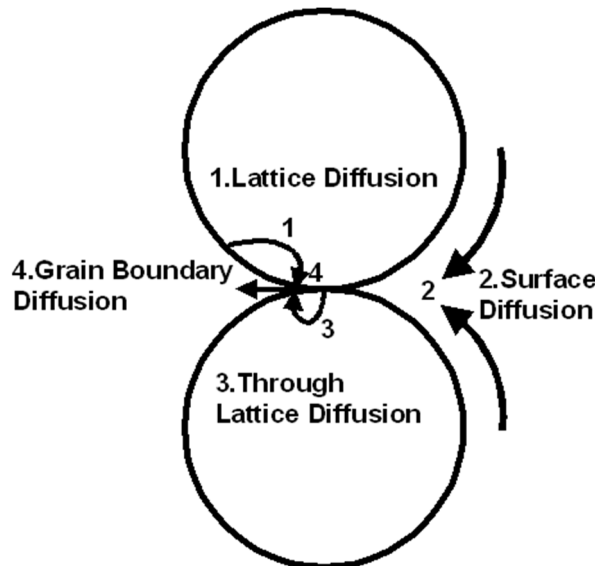


Figure 5. A schematic is representing various atomic diffusion paths between two contacting particles. Reprinted with permission from Ref. [31].

In the initial stage, the interparticle neck forms and increases the particle contact area [30]. Neck growth is the dominant factor that reduces the resistivity of sintered particles because it increases the cross-sectional contact area between the particles [32]. As the temperature is increased, the nanoparticles start forming dense agglomerates due to the fusion of particles caused by surface diffusion, grain boundary diffusion, as well as lattice diffusion [33]. The neck formation is driven by surface energy reduction due to the particles' large surface-to-volume ratio, a process known as Ostwald ripening [34]. Ostwald ripening triggers the diffusion mechanisms, which enables more contact between the fused particles. Grain boundary diffusion allows for neck formation and neck radii increase.

Besides neck growth between several particles, percolation networks emerge due to multi-particle-related sintering [35]. These percolation networks create an electron flow path, thereby decreasing the resistivity of the pattern. The surface of Ag nanoparticles provides a sufficient path for electron flow. Finally, a coalesced densified, non-porous metallic pattern emerges on the substrate. For the sample sintered at 250 °C, the resistivity dropped rapidly during the initial stage of sintering (from 10 to 20 min) due to the earlier neck formation and faster neck growth. As the sintering process gets closer to the intermediate stage, the variation of resistivity between different times became smaller, as the rate of neck growth decreases. For temperatures above 300 °C, the rapid drop of resistivity happens around 10 min. As the sintering process gets closer to the intermediate stage, the difference in resistivity becomes smaller, since the rate of neck growth decreases during the sintering process.

Resistivities at all temperatures fall slowly at the intermediate stage of sintering due to the relatively slow rate of neck growth and coalescence of the particles. From Figure 6, it is evident that the thickness of the pattern increases with the number of printed layers.

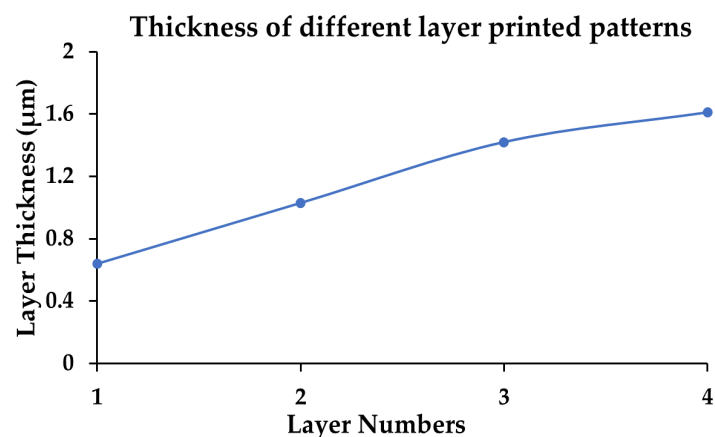


Figure 6. Thickness of printed pattern as a function of printed layers.

Though a thicker pattern could result in well-connected conductive pathways resulting in slightly improved conductivity (refer Table 3), the trade-off between ink consumption (cost) and electrical conductivity should not be ignored. In this context, the authors chose the conductivity of 3 L printing at 300 °C sintering temperature for 30 min as the optimum process parameter for inkjet printing. As sintering enables the nanoparticles to coalesce together, densification occurs in vertical and horizontal directions. The thickness of the printed layer did not increase linearly with an increase in the printing layer as the densification process seems non-uniform. The thickness of the pattern was measured using a cross-sectional SEM analysis. Figure 7 shows a thickness of 1.61 µm for the four-layer printed pattern. The image appears to show a good adhesion of silver nanoparticles with the substrate.

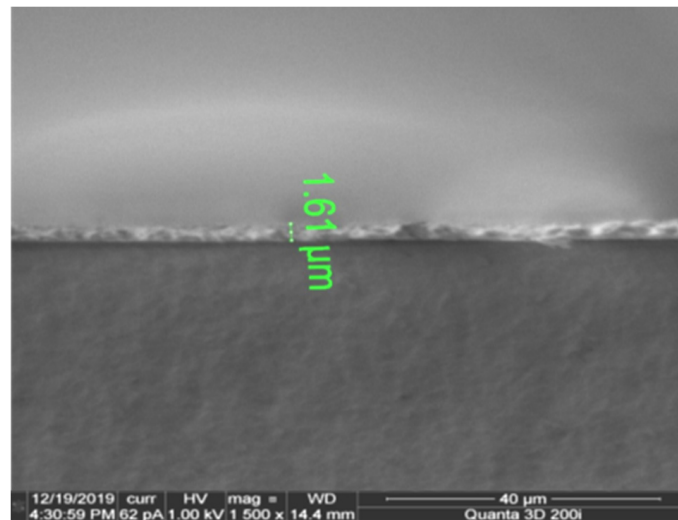


Figure 7. Thickness of 4-layer printed samples using SEM.

3.2. Surface Characterization

The surface morphology of the printed pattern was studied using SEM images. Figure 8 shows the SEM images of the printed patterns (different layers) sintered at 300 °C.

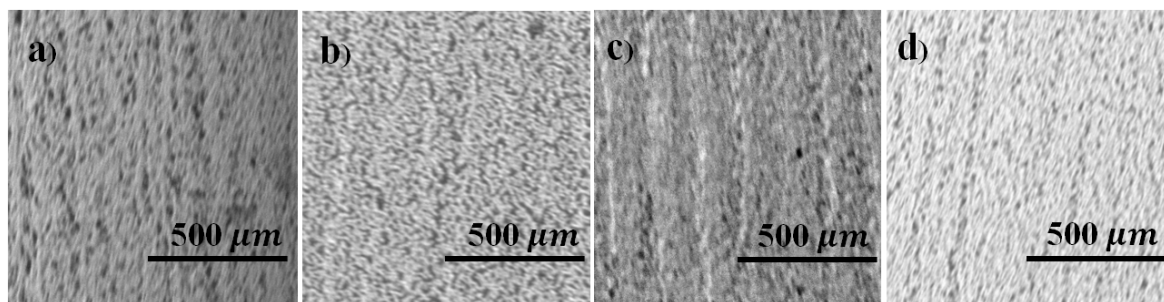


Figure 8. Surface morphology of the printed patterns sintered at 300 °C: (a) 1 L, (b) 2 L, (c) 3 L, (d) 4 L sintered at 300 °C.

Figure 8a shows the single-layer printed pattern containing a lot of holes and uneven edges. The surface of the double layer printed pattern is depicted in Figure 8b. Through visual inspection, it seems that the image of a double layer printed pattern has fewer holes than the single-layered one. The number density of holes seems to decrease with an increase in the number of printed layers (calculated based on 1 μm square box and counting them). The printing quality appears to be superior for 4 L, as shown in Figure 8d. The 2D RMS surface roughness was computed using Alpha-Step[®] D-300 Stylus Profile. Figure 9 shows the average and RMS surface roughness values as a function of the number of layers of the printed pattern before and after sintering at 300 °C. Before sintering, the roughness of the surface seems quite high, but the value seems to decrease after sintering. The surface roughness value seems to be small for a double layer printed pattern before and after sintering and continues to decrease with the number of layers. A thicker pattern is believed to allow more time for the capillary re-flow of ink, thereby creating a smooth top layer [36].

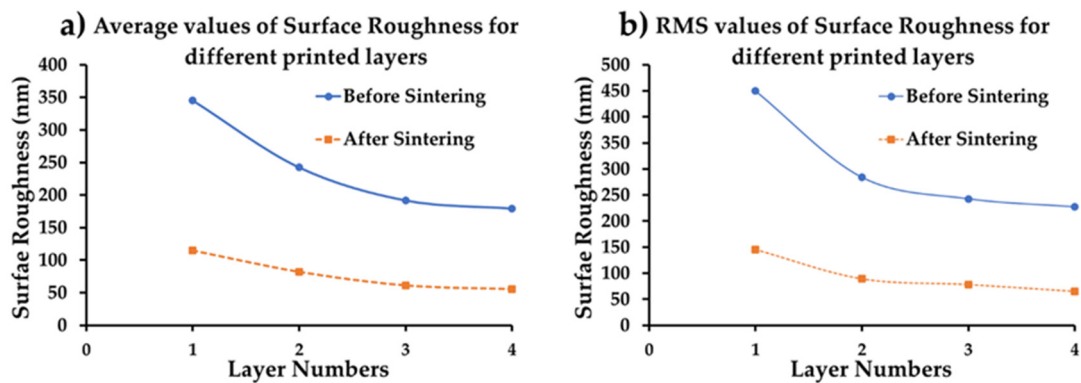


Figure 9. Surface roughness plot for different printed layers before and after sintering (a) Average value of surface roughness value, and (b) RMS value of surface roughness.

3.3. High-Temperature Tolerance

The image of the printed capacitor pattern on the ceramic substrate for high temperature testing is shown in Figure 10a. After sintering the printed IDT capacitor, the measured capacitance value was found to be 46.5 pF (Figure 10b), indicating the electrical integrity of the IDT pattern. The slight difference in capacitance between the simulation (48 pF) and the experiment is attributed to imperfections in fabrication. After heating for an hour (Figure 10c), the capacitance value was found to be 52.9 pF after the substrate cooled down, indicating the absence of any degradation when subjected to high temperatures. Being a dielectric material, the dielectric constant of E-strate[®] increases with the increase of temperature under a constant frequency [37]. The increase in capacitance after the substrate was cooled is attributed to the temperature-dependent dielectric properties of the ceramic. The temperature was limited to 500 °C due to the presence of Ag ink. Device testing at higher temperatures is possible when high-temperature tolerant inks such as Pt is used.

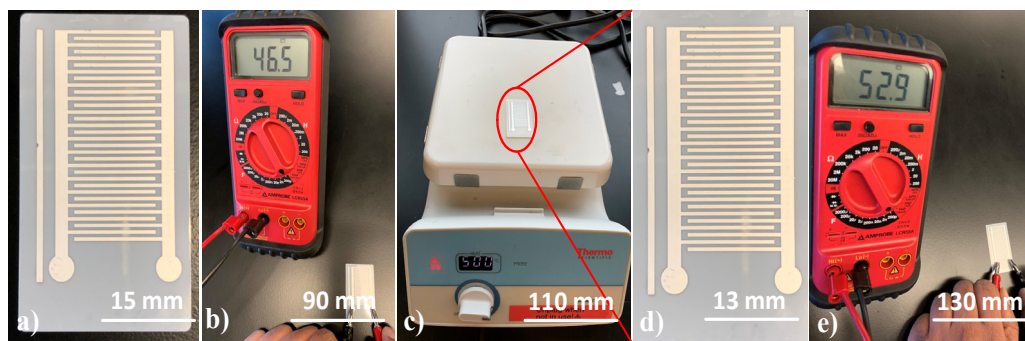


Figure 10. High-temperature stability test results (a) Interdigitated capacitive pattern after sintering, (b) Measuring capacitance using LCR meter, (c) Heating on the hotplate at 500 °C, (d) Capacitive pattern after one-hour heating, and (e) Measuring capacitance using LCR meter after heating.

3.4. Flexibility and Adhesion Test Result

The electrical resistivity was measured during and after repetitive bending. No cracks or deformation have been found after bending. A 3% change in resistivity was observed after repeated flexes (100 runs), enabling its use in flexible sensors and antenna applications. The adhesion of the Ag ink on the thin E-strate[®] was inspected using the ASTM tape test. The surface of the substrate after the tape pull off was recorded using the Fiducial camera of the DMP-2831 printer (Figure 11). Edges of the cut were smooth with some ink detachments. Less than 5% of the test area was seen to detach due to tape pull off. Hence, the substrate is classified into a class 4B adhesion rating [38]. The sintering temperature was kept at least 250 °C for proper adhesion according to AgNP ink datasheet. A high-temperature adhesion test (using fiberglass tape) was performed at 500 °C, and the absence of

significant detachment (figure not shown) was noted. Several other factors might affect adhesion, for instance, surface roughness, surface energy, and polarities of the contact surfaces, and the porosity of the substrate surfaces [39]. Sintering temperature and sintering time are other dominant factors affecting the adhesion of printed patterns on non-porous substrates [40]. The bending and adhesion tests indicate a well-sintered pattern, which is mechanically and electrically stable, conducive for implementing flexible devices for IoT applications.

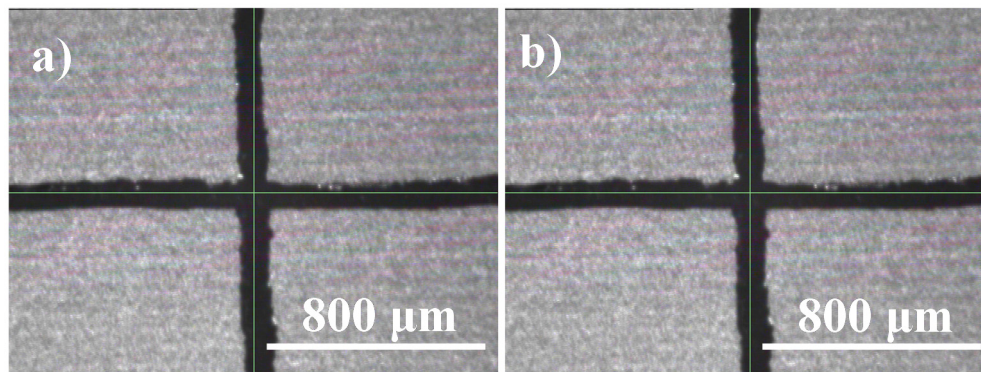


Figure 11. ASTM tape test: (a) before tape test (b) image after tape pull of using Fiducial camera.

4. Conclusions

In this article, the optimization of inkjet printing properties on a new ceramic substrate has been reported. The impact of drop spacing, number of printing layers, sintering temperature, and sintering time on the resistivity of the pattern was studied. The number of printing layers, sintering temperature, and their interaction were found to be significant factors affecting the electrical conductivity of the printed pattern. The optimum printing parameters for the thin E-strate[®] substrate were found to be 20 μm drop spacing, three layers of printing, and 300 $^{\circ}\text{C}$ sintering temperature for 30 min. The physics of resistivity evolution during sintering has been discussed. The printed sample was found to exhibit high-temperature tolerance with adequate flexibility and adhesion to the substrate. These results indicate the suitability of the ceramic substrate for multi-functional flexible and wearable sensors for IoT applications.

Author Contributions: Conceptualization, P.K.S. and K.S.; methodology, S.G.K. and M.A.R.; formal analysis, S.G.K.; investigation, S.G.K. and M.A.R.; resources, P.K.S. and K.S.; data curation, S.G.K.; writing—original draft preparation, S.G.K. and M.A.R.; writing—review and editing, P.K.S., S.U.K., A.W.; visualization, A.W., S.U.K.; supervision, P.K.S., A.W., and S.U.K.; project administration, P.K.S. All authors have read and agreed to the published version of the manuscript.

Funding: This research received no external funding.

Acknowledgments: The authors thank Kathy Olenick and John Olenick for EnrG Inc. for technical advice.

Conflicts of Interest: The authors declare no conflict of interest.

References

1. Meng, K.; Zhao, S.; Zhou, Y.; Wu, Y.; Zhang, S.; He, Q.; Wang, X.; Zhou, Z.; Fan, W.; Tan, X.; et al. A Wireless Textile-Based Sensor System for Self-Powered Personalized Health Care. *Matter* **2020**, *2*, 896–907. [[CrossRef](#)]
2. He, Y.; Shi, X.; Chen, K.; Yang, X.; Chen, J. Titanium-Doped P-Type WO_3 Thin Films for Liquefied Petroleum Gas Detection. *Nanomaterials* **2020**, *10*, 727. [[CrossRef](#)] [[PubMed](#)]
3. Zhang, N.; Tao, C.; Fan, X.; Chen, J. Progress in Triboelectric Nanogenerators as Self-powered Smart Sensors. *J. Mater. Res.* **2017**, *32*, 1628–1646. [[CrossRef](#)]
4. Martin, P.G.; Tomkinson, N.G.; Scott, T.B. The Future of Nuclear Security: Commitments and Actions—Power Generation and Stewardship in the 21st Century. *Energy Policy* **2017**, *110*, 325–330. [[CrossRef](#)]

5. Milligan, W.J.; Poli, G.; Harrison, D.K. The Integration of an API619 Screw Compressor Package into the Industrial Internet of Things. *IOP Conf. Ser. Mater. Sci. Eng.* **2017**, *232*, 012088. [[CrossRef](#)]
6. Krasniqi, X.; Hajrizi, E. Use of IoT Technology to Drive the Automotive Industry from Connected to Full Autonomous Vehicles. *IFAC-PapersOnLine* **2016**, *49*, 269–274. [[CrossRef](#)]
7. Liu, Y.; Kashef, M.; Lee, K.B.; Benmohamed, L.; Candell, R. Wireless Network Design for Emerging IIoT Applications: Reference Framework and Use Cases. *Proc. IEEE* **2019**, *107*, 1166–1192. [[CrossRef](#)]
8. Fraga-Lamas, P.; Fernández-Caramés, T.; Suárez-Albela, M.; Castedo, L.; González-López, M. A Review on Internet of Things for Defense and Public Safety. *Sensors* **2016**, *16*, 1644. [[CrossRef](#)]
9. Ohodnicki, P.R.; Credle, S.; Buric, M.; Lewis, R.; Seachman, S. *High Temperature, Harsh Environment Sensors for Advanced Power Generation Systems*; George, T., Dutta, A.K., Islam, M.S., Eds.; International Society for Optics and Photonics: Baltimore, MD, USA, 2015; p. 94671M.
10. Raza, M.; Aslam, N.; Le-Minh, H.; Hussain, S.; Cao, Y.; Khan, N.M. A Critical Analysis of Research Potential, Challenges, and Future Directives in Industrial Wireless Sensor Networks. *IEEE Commun. Surv. Tutor.* **2018**, *20*, 39–95. [[CrossRef](#)]
11. Cruz, S.M.F.; Rocha, L.A.; Viana, J.C. Printing Technologies on Flexible Substrates for Printed Electronics. In *Flexible Electronics*; Rackauskas, S., Ed.; InTech: London, UK, 2018; ISBN 978-1-78923-456-5.
12. Khan, S.; Lorenzelli, L.; Dahiya, R.S. Technologies for Printing Sensors and Electronics Over Large Flexible Substrates: A Review. *IEEE Sens. J.* **2015**, *15*, 3164–3185. [[CrossRef](#)]
13. Aryal, M.; Allison, S.W.; Olenick, K.; Sabri, F. Flexible thin film ceramics for high temperature thermal sensing applications. *Opt. Mater.* **2020**, *100*, 109656. [[CrossRef](#)]
14. Zhang, Y.; Sun, S.; Pratap, R.; Galstyan, E.; Wosik, J.; Selvamanickam, V. Development of REBCO Tapes on Nonmetallic Flexible Substrates for RF Applications. *IEEE Trans. Appl. Supercond.* **2019**, *29*, 1–5. [[CrossRef](#)]
15. Fobare, D.; Haldar, P.; Efstathiadis, H.; Metacarpa, D.; Wax, J.; Olenick, J.; Olenick, K.; Venkateswaran, V. Novel Application of Ytria Stabilized Zirconia as a Substrate for Thin Film CIGS Solar Cells. In Proceedings of the 2014 IEEE 40th Photovoltaic Specialist Conference (PVSC), Denver, CO, USA, 8–13 June 2014.
16. de Cos Gómez, M.E.; Fernández Álvarez, H.; Puerto Valcarce, B.; García González, C.; Olenick, J.; Las-Heras Andrés, F. Zirconia-Based Ultra-Thin Compact Flexible CPW-Fed Slot Antenna for IoT. *Sensors* **2019**, *19*, 3134. [[CrossRef](#)] [[PubMed](#)]
17. You, R.; Jing, G.; Yu, H.; Cui, T. Flexible Mixed-Potential-Type (MPT) NO₂ Sensor Based on an Ultra-Thin Ceramic Film. *Sensors* **2017**, *17*, 1740. [[CrossRef](#)] [[PubMed](#)]
18. Raut, N.C.; Al-Shamery, K. Inkjet Printing Metals on Flexible Materials for Plastic and Paper Electronics. *J. Mater. Chem. C* **2018**, *6*, 1618–1641. [[CrossRef](#)]
19. Yu, J.H.; Rho, Y.; Kang, H.; Jung, H.S.; Kang, K.-T. Electrical behavior of laser-sintered Cu based metal-organic decomposition ink in air environment and application as current collectors in supercapacitor. *Int. J. Precis. Eng. Manuf.-Green Tech.* **2015**, *2*, 333–337. [[CrossRef](#)]
20. Vandevenne, G.; Marchal, W.; Verboven, I.; Drijkoningen, J.; D’Haen, J.; Van Bael, M.K.; Hardy, A.; Deferme, W. A Study on the Thermal Sintering Process of Silver Nanoparticle Inkjet Inks to Achieve Smooth and Highly Conducting Silver Layers: Thermal Sintering Process of Silver Nanoparticle Inkjet Inks. *Phys. Status Solidi A* **2016**, *213*, 1403–1409. [[CrossRef](#)]
21. Gamerith, S.; Klug, A.; Scheiber, H.; Scherf, U.; Moderegger, E.; List, E.J.W. Direct Ink-Jet Printing of Ag-Cu Nanoparticle and Ag-Precursor Based Electrodes for OFET Applications. *Adv. Funct. Mater.* **2007**, *17*, 3111–3118. [[CrossRef](#)]
22. Mo, L.; Guo, Z.; Yang, L.; Zhang, Q.; Fang, Y.; Xin, Z.; Chen, Z.; Hu, K.; Han, L.; Li, L. Silver Nanoparticles Based Ink with Moderate Sintering in Flexible and Printed Electronics. *IJMS* **2019**, *20*, 2124. [[CrossRef](#)]
23. Ding, J.; Liu, J.; Tian, Q.; Wu, Z.; Yao, W.; Dai, Z.; Liu, L.; Wu, W. Preparing of Highly Conductive Patterns on Flexible Substrates by Screen Printing of Silver Nanoparticles with Different Size Distribution. *Nanoscale Res. Lett.* **2016**, *11*, 412. [[CrossRef](#)] [[PubMed](#)]
24. Riheen, M.A.; Saha, T.K.; Sekhar, P.K. Inkjet Printing on PET Substrate. *J. Electrochem. Soc.* **2019**, *166*, B3036–B3039. [[CrossRef](#)]
25. Saha, T.K.; Knaus, T.N.; Khosla, A.; Sekhar, P.K. Investigation of Printing Properties on Paper Substrate. *J. Electrochem. Soc.* **2018**, *165*, B3163–B3167. [[CrossRef](#)]
26. Topsoe, H. Geometric Factors in Four Point Resistivity Measurement. *Bulletin* **1968**, *472*, 63.

27. Tran, D.-P.; Lu, H.-I.; Lin, C.-K. Conductive Characteristics of Indium Tin Oxide Thin Film on Polymeric Substrate under Long-Term Static Deformation. *Coatings* **2018**, *8*, 212. [[CrossRef](#)]
28. Liu, H.; Wen, P.; Zhu, S.; Ren, B.; Guan, X.; Yu, H. Quad-Band CPW-Fed Monopole Antenna Based on Flexible Pentangle-Loop Radiator. *Antennas Wirel. Propag. Lett.* **2015**, *14*, 1373–1376.
29. Chinga-Carrasco, G.; Tobjörk, D.; Österbacka, R. Inkjet-printed Silver Nanoparticle on Nano-engineered Cellulose Films for Electrically Conducting Structures and Organic Transistors: Concept and Challenges. *J. Nanopart. Res.* **2012**, *14*, 1213. [[CrossRef](#)]
30. German, R.M. Thermodynamics of Sintering. In *Sintering of Advanced Materials*; Elsevier: Amsterdam, The Netherlands, 2010; pp. 3–32. ISBN 978-1-84569-562-0.
31. Greer, J.R.; Street, R.A. Thermal Cure Effects on Electrical Performance of Nanoparticle Silver Inks. *Acta Mater.* **2007**, *55*, 6345–6349. [[CrossRef](#)]
32. Zhang, Y.; Wu, L.; Guo, X.; Jung, Y.-G.; Zhang, J. Molecular Dynamics Simulation of Electrical Resistivity in Sintering Process of Nanoparticle Silver Inks. *Comput. Mater. Sci.* **2016**, *125*, 105–109. [[CrossRef](#)]
33. Ingham, B.; Lim, T.H.; Dotzler, C.J.; Henning, A.; Toney, M.F.; Tilley, R.D. How Nanoparticles Coalesce: An In Situ Study of Au Nanoparticle Aggregation and Grain Growth. *Chem. Mater.* **2011**, *23*, 3312–3317. [[CrossRef](#)]
34. Perelaer, J.; Smith, P.J.; Mager, D.; Soltman, D.; Volkman, S.K.; Subramanian, V.; Korvink, J.G.; Schubert, U.S. Printed Electronics: The Challenges Involved in Printing Devices, Interconnects, and Contacts Based on Inorganic Materials. *J. Mater. Chem.* **2010**, *20*, 8446. [[CrossRef](#)]
35. Choi, J.H.; Ryu, K.; Park, K.; Moon, S.-J. Thermal Conductivity Estimation of Inkjet-printed Silver Nanoparticle Ink during Continuous Wave Laser Sintering. *Int. J. Heat Mass Transf.* **2015**, *85*, 904–909. [[CrossRef](#)]
36. Nguyen, H.-A.-D.; Lee, C.; Shin, K.-H. A Mathematical Model to Predict Surface Roughness and Pattern Thickness in Roll-to-roll Gravure Printed Electronics. *Robot. Comput.-Integr. Manuf.* **2013**, *29*, 26–32. [[CrossRef](#)]
37. Lanagan, M.T.; Yamamoto, J.K.; Bhalla, A.; Sankar, S.G. The Dielectric Properties of Yttria-stabilized Zirconia. *Mater. Lett.* **1989**, *7*, 437–440. [[CrossRef](#)]
38. ASTM International. *D01 Committee Test Methods for Rating Adhesion by Tape Test*; ASTM International: West Conshohocken, PA, USA, 2017.
39. Merilampi, S.; Laine-Ma, T.; Ruuskanen, P. The Characterization of Electrically Conductive Silver Ink Patterns on Flexible Substrates. *Microelectron. Reliab.* **2009**, *49*, 782–790. [[CrossRef](#)]
40. Halonen, E.; Viiru, T.; Ostman, K.; Cabezas, A.L.; Mantysalo, M. Oven Sintering Process Optimization for Inkjet-Printed Ag Nanoparticle Ink. *IEEE Trans. Compon. Packag. Manuf. Technol.* **2013**, *3*, 350–356. [[CrossRef](#)]



© 2020 by the authors. Licensee MDPI, Basel, Switzerland. This article is an open access article distributed under the terms and conditions of the Creative Commons Attribution (CC BY) license (<http://creativecommons.org/licenses/by/4.0/>).